Research Square

Preprints are preliminary reports that have not undergone peer review.
They should not be considered conclusive, used to inform clinical practice,
or referenced by the media as validated information.

Application of modified phosphogypsum for efficient removal of methyl blue from aqueous solutions

Zhihao Fang

wfsgfzh@163.com

Weifang University of Science and Technology

Mengjie Bai

Weifang University of Science and Technology

Jiangbo Yu

Shenyang University of Chemical Technology

Wenxu Wang

Shenyang University of Chemical Technology

Yiqing Jiao

Weifang University of Science and Technology

Yongwei Li

Weifang University of Science and Technology

Shuyu Zhang

Hubei University

Xinwei Li

Shenyang University of Chemical Technology

Mengxue Yuan

Weifang University of Science and Technology

Xiao Yang

Weifang University of Science and Technology

Shuyan Zang

Shenyang University of Chemical Technology

Chengjie Li

Weifang University of Science and Technology

Research Article

Keywords: Phosphogypsum, Cetyltrimethylammonium bromide, Methyl blue, Microwave-assisted synthesis, Adsorption, Isosteric thermodynamics

Posted Date: November 27th, 2026

DOI: https://doi.org/10.21203/rs.3.rs-11647019/v1

License: This work is licensed under a Creative Commons Attribution 4.0 International License.
Read Full License

Additional Declarations: No competing interests reported.

Application of modified phosphogypsum for efficient removal of methyl blue from aqueous solutions

Zhihao Fang[a], Mengjie Bai[a], Jiangbo Yu[a,b], Wenxu Wang[a,b], Yiqing Jiao[a], Yongwei Li[a], Shuyu Zhang[c], Xinwei Li[a,b], Mengxue Yuan[a], Xiao Yang[a], Shuyan Zang[b,*], Chengjie Li[a,*]

[a] Shandong Engineering Research Center of Green and High-value Marine Fine Chemical, Weifang Engineering Laboratory for Clean Utilization of Chemical Resources. Weifang University of Science and Technology, Weifang 262700, China

[b] College of Science, Shenyang University of Chemical Technology, Shenyang 110142, China

[c] Manchester Metropolitan Joint Institute, Hubei University, Wuhan 430062, China

* Correspondence: Shuyan Zang (zangshuyan@126.com); Chengjie Li (cjli@wfust.edu.cn)

Author contributions

Zhihao Fang: Conceptualization, Methodology, Formal analysis, Writing – original draft. Mengjie Bai: Investigation, Formal analysis, Writing – original draft. Jiangbo Yu: Writing – original draft, Writing – review & editing. Wenxu Wang: Formal analysis, Writing – original draft. Yiqing Jiao: Investigation, Formal analysis. Yongwei Li: Investigation, Formal analysis. Shuyu Zhang: Formal analysis. Xinwei Li: Investigation, Formal analysis. Mengxue Yuan: Writing – review & editing. Xiao Yang: Writing – review & editing. Shuyan Zang: Methodology, Formal analysis. Chengjie Li: Writing – review & editing. All authors approved the final version of the manuscript.

Abstract

Phosphogypsum (PG), an abundant industrial solid waste, is a promising substrate for dye remediation through interfacial modification. Herein, cetyltrimethylammonium bromide (CTAB)-modified PG (CTAB@PG) was prepared via a microwave-assisted hydrothermal route and applied for the removal of methyl blue (MB), an anionic triarylmethane dye. Under identical adsorption conditions, CTAB modification increased MB uptake by 124.6%, from 215.0 to 482.8 $mg \cdot g^{-1}$, despite a 55.7% decrease in specific surface area from 20.92 to 9.27 $m^2 \cdot g^{-1}$. CTAB@PG achieved 96.6% removal within 20 min at 298 K and pH 6, using an adsorbent dosage of 0.02 g in 50 mL of 200 $mg \cdot L^{-1}$ MB solution. The kinetic data were well described by the pseudo-second-order model, while the Freundlich isotherm provided the best fit to the equilibrium data ($R^2 > 0.99$), consistent with heterogeneous adsorption. Fixed-loading thermodynamic analyses based on Freundlich and Langmuir isotherms yielded positive transfer enthalpies of 17.16–17.96 $kJ \cdot mol^{-1}$, with relative differences below 3% at matched loadings, demonstrating consistent endothermic behavior across both models. Furthermore, CTAB@PG retained approximately 90% removal efficiency after six regeneration cycles using 0.1 $mol \cdot L^{-1}$ NaOH. Enhanced uptake was attributed to electrostatic attraction between CTAB-derived quaternary ammonium groups and dye sulfonate groups, complemented by hydrophobic association with alkyl-rich regions. These findings highlight the role of interfacial modification in enhancing dye uptake and demonstrate a route for converting PG into a reusable adsorbent.

Keywords: Phosphogypsum; Cetyltrimethylammonium bromide; Methyl blue; Microwave-assisted synthesis; Adsorption; Isosteric thermodynamics

1. Introduction

Textile dyeing wastewater combines high chromaticity with complex chemical compositions and the persistence of many synthetic dyes, making effective treatment an environmental priority (Deshmukh et al. 2025; Sahu and Poler 2024). Advanced oxidation, membrane separation, electrochemical treatment, and biological processes address this problem through different removal or transformation pathways (Deshmukh et al. 2025; Lin et al. 2024; Sahu and Poler 2024). Their application nevertheless depends on managing membrane fouling and concentrated waste streams, energy and chemical inputs, or the limited biodegradability of some dyes (Deshmukh et al. 2025; Lin et al. 2024; Sahu and Poler 2024). Against this background, adsorption offers a comparatively simple route for capturing dye molecules, provided that the adsorbent maintains useful uptake and can be regenerated (Ahmed et al. 2026; Hosny et al. 2023).

The development of such adsorbents therefore requires attention to both accessible adsorption sites and the chemical interactions that govern dye binding. Mineral-based materials, carbonaceous adsorbents, polymeric composites, and surfactant-functionalized materials illustrate different ways of adjusting these properties (Ahmed et al. 2026; Bulin et al. 2024; Dang et al. 2024; Hosny et al. 2023; Mostafa et al. 2023; Vaid et al. 2024). In particular, surfactant functionalization can introduce charged groups and organic domains at the solid–water interface, providing opportunities to tailor interactions with dye molecules (Ahmed et al. 2026; Dang et al. 2024; Mostafa et al. 2023; Vaid et al. 2024). This emphasis on surface chemistry also motivates the use of mineral wastes as substrates: their value for dye removal can depend on how effectively their interfaces are modified, rather than on their initial pore structure alone.

PG, a calcium-sulfate-rich by-product of wet-process phosphoric acid production, is one such substrate. Its use as an adsorbent enables dye removal while valorizing an industrial

secondary resource (Alotaibi et al. 2025; Hu et al. 2025; Shao et al. 2026). Recent studies have explored PG surface functionalization for the adsorption of metals and dyes (Hu et al. 2025), while investigations of cationic-surfactant-assisted PG transformation show that these modifiers interact with PG-derived surfaces during treatment (Wang et al. 2024). More directly, Lu et al. used surfactant-modified PG to remove anionic dyes, including MB, and identified electrostatic and hydrophobic interactions among the adsorption pathways (Lu et al. 2023). These results establish a basis for examining how the modification route influences the balance between pore accessibility and interfacial affinity in PG-based adsorbents.

Microwave-assisted treatment provides an alternative preparation route for exploring this balance. Conventional hydrothermal treatment for 3 h has been used in surfactant-assisted PG crystal transformation (Wang et al. 2024). In a separate comparison using *Luffa cylindrica*, microwave assistance shortened CTAB functionalization and enhanced anionic-dye adsorption (Bouzaabia et al. 2025). These findings provide a rationale for investigating microwave-assisted CTAB treatment of PG. The relevant questions are how this treatment changes the PG interface, whether the resulting changes improve MB uptake when considered alongside the measured surface area, and whether the adsorption performance persists after regeneration.

To address these questions, CTAB@PG was prepared by microwave-assisted treatment, and its structural, surface, and adsorption properties were compared with those of PG. Particular attention was paid to the relationship between accessible surface area and MB uptake to clarify the contribution of interfacial modification to adsorption enhancement. Batch experiments examined the effects of pH, concentration, dosage, contact time, temperature, and coexisting ions. Kinetic and equilibrium analyses characterized the adsorption response, while fixed-loading thermodynamic analyses based on Freundlich and Langmuir representations were compared at matched loadings to assess the consistency of the

inferred temperature dependence. Repeated adsorption–desorption experiments further evaluated the recoverability of the adsorption function. Together, these analyses connect interfacial modification with enhanced MB affinity, consistent endothermic transfer, and retained performance after regeneration.

2. Experimental

2.1 Materials and instruments

All chemical reagents employed in this study were of analytical grade. PG powder was obtained from Hangzhou, Zhejiang Province, China. MB ($C_{37}H_{27}N_3O_9S_3 \cdot 2Na$) was purchased from Aladdin Biochemical Technology Co., Ltd. (Shanghai, China), and CTAB ($C_{19}H_{42}BrN$) from Macklin Biochemical Co., Ltd. (Shanghai, China). HCl, NaOH, KCl, $ZnCl_2$, $CaCl_2$, $NaNO_3$, NaCl, and Na_2SO_4 were purchased from Shanghai Yuanye Bio-Technology Co., Ltd. (Shanghai, China). HCl and NaOH were used for pH adjustment, and NaOH was also used for adsorbent regeneration. KCl, $ZnCl_2$, $CaCl_2$, $NaNO_3$, NaCl, and Na_2SO_4 were used in the coexisting-ion experiments. Deionized (DI) water was used for solution preparation and washing. Sample filtration used 0.22 μm polyethersulfone (PES) membranes, and N_2 was used as the atmosphere for thermal analysis and the adsorptive gas for porosity measurements.

Microwave-assisted preparation used a microwave reactor (XH-MC-1, Beijing Xianghu Science & Technology Development Co., Ltd., China) fitted with a sealed 35 mL TFM vessel. Characterization instruments were a Fourier transform infrared (FT-IR) spectrometer (FTIR-650, Tianjin Gangdong Science & Technology Development Co., Ltd.), a scanning electron microscope (SEM; ZEISS Sigma 360, Germany), an X-ray diffractometer (XRD; Rigaku Ultima IV, Japan), a surface-area and porosity analyzer (Micromeritics ASAP 2460, USA), and a thermal analyzer (Hitachi STA200, Japan). MB concentrations were measured

using a UV–visible (UV-Vis) spectrophotometer (752N, Shanghai Analytical Instrument Co., Ltd.).

2.2 Preparation of CTAB@PG

CTAB@PG was prepared using a microwave-assisted hydrothermal method. PG was first washed three times with DI water to remove soluble impurities, filtered, dried at 60 °C, ground, and sieved through a 200-mesh screen.

Pretreated PG (1.000 g) and CTAB (0.020 g) were dispersed in 30 mL of DI water and magnetically stirred for 60 min. The suspension was transferred to a sealed 35 mL TFM vessel and treated in the microwave reactor at a constant power of 150 W and a frequency of 2.5 GHz. The temperature was raised to 200 °C and maintained for 60 min under autogenous pressure. The vessel was allowed to cool naturally to room temperature before opening.

The resulting precipitate was collected by centrifugation at 8000 rpm for 5 min and washed three times with DI water to remove residual CTAB and soluble by-products. The material was then vacuum-dried at 60 °C for 12 h.

2.3 Characterization

PG and CTAB@PG were characterized under the same measurement conditions. FT-IR spectra were recorded over 500–4000 cm^{-1} to examine surface functional groups, and SEM was used to observe surface morphology. XRD patterns were collected using Cu Kα radiation (λ = 1.5418 Å) at 40 kV and 40 mA to identify crystalline phases. N_2 adsorption–desorption measurements were used to determine Brunauer–Emmett–Teller (BET) specific surface areas and Barrett–Joyner–Halenda (BJH) pore-size distributions. Thermal behavior was examined by thermogravimetric analysis (TGA) under N_2 from 30 to 800 °C at a heating rate of 10 °C·min^{-1}. The instruments are listed in Section 2.1.

2.4 Batch adsorption experiments

Batch adsorption experiments were conducted in 100 mL Erlenmeyer flasks containing 50 mL of MB solution and agitated at 220 rpm in a temperature-controlled water-bath shaker. The initial solution pH was adjusted with 0.1 mol·L^{-1} HCl or NaOH. Unless otherwise stated, the working conditions were an initial MB concentration of 200 mg·L^{-1}, a CTAB@PG dosage of 0.020 g, an initial pH of 6, a temperature of 298 K, and a contact time of 20 min. PG and CTAB@PG were compared under identical conditions.

After the prescribed contact time, a 2.0 mL aliquot was filtered through a 0.22 μm PES membrane. The residual MB concentration was determined by UV-Vis spectrophotometry at its maximum absorption wavelength (λmax = 595 nm). Samples outside the linear calibration range were diluted with DI water before measurement, and the dilution factor was included in the concentration calculation. All experiments were performed in triplicate, and the error bars represent the standard deviation of the three measurements (n = 3). Equilibrium adsorption capacity and removal efficiency were calculated from the mass balance using Equations (1) and (2) (Hidayat et al. 2024).

$$q_e(\text{mg}\cdot\text{g}^{-1}) = \frac{C_0 - C_e}{m} \times V \quad (1)$$

$$R(\%) = \frac{C_0 - C_e}{C_0} \times 100\% \quad (2)$$

The initial and equilibrium concentrations of the dye in the solution are denoted as C_0 and C_e (mg·L^{-1}), respectively. The adsorption capacity at equilibrium, represented as q_e (mg·g^{-1}), corresponds to the amount of dye adsorbed per unit mass of adsorbent. Other parameters include V (L), which is the volume of the dye solution, and m (g), the mass of the adsorbent used.

Individual operating variables were examined while maintaining the other baseline conditions specified above. Initial pH values of 2, 4, 6, 8, and 10 were investigated. Initial MB concentrations were 20, 50, 100, 200, and 300 mg·L^{-1}, and CTAB@PG dosages were

0.01, 0.02, 0.03, 0.04, and 0.05 g. Contact-time measurements were performed at 1, 3, 5, 10, 15, 20, and 40 min. The temperature series comprised 298, 313, 323, 333, and 353 K. The working conditions were selected by considering removal efficiency, uptake per unit mass, contact time, and temperature within these investigated ranges.

2.5 Kinetic, equilibrium, and thermodynamic analyses

Kinetic experiments were conducted at an initial MB concentration of 200 $mg \cdot L^{-1}$ and temperatures of 298, 313, and 333 K, using the solution volume, dosage, pH, and agitation conditions described in Section 2.4. The time-dependent uptake data were analyzed using the pseudo-first-order (PFO), pseudo-second-order (PSO), and Weber–Morris intraparticle diffusion models. The equations and fitted parameters are presented in Section 3.3, Table 1, Fig. S2, and Table S2.

Equilibrium isotherms were measured at 298, 313, and 333 K at different initial MB concentrations and a contact time of 20 min. The solution volume, adsorbent dosage, initial pH, and agitation rate were maintained as specified in Section 2.4. Langmuir, Freundlich, Temkin, and Dubinin–Radushkevich (D–R) models were fitted to the equilibrium data; their equations and parameters are presented in Section 3.4 and Table 2.

For thermodynamic analysis, each isotherm representation was inverted to calculate equilibrium concentrations at fixed loadings within the common experimental range of the three temperatures (150–600 $mg \cdot g^{-1}$). The concentrations were converted from $mg \cdot L^{-1}$ to $mol \cdot L^{-1}$ using an MB molar mass of 799.81 $g \cdot mol^{-1}$. Differential molar transfer parameters relative to the ideal solution standard state (C° = 1 $mol \cdot L^{-1}$) were obtained by ordinary least-squares regression of $\ln(C_e/C^\circ)$ against 1/T at each loading. Freundlich- and Langmuir-derived results were compared at the same loadings and reference state. Definitions, equations, and numerical results are given in Section 3.5 and Sections S2–S3 of the Supporting Information.

2.6 Coexisting ion experiments

The influence of coexisting ions was evaluated using KCl, $ZnCl_2$, and $CaCl_2$ as the sources of K^+, Zn^{2+}, and Ca^{2+}, respectively, and $NaNO_3$, NaCl, and Na_2SO_4 as the sources of NO_3^-, Cl^-, and SO_4^{2-}. Each salt was examined separately at coexisting-ion concentrations of 0, 300, 600, and 900 $mg \cdot L^{-1}$. For each test, 0.020 g of CTAB@PG was added to 50 mL of 200 $mg \cdot L^{-1}$ MB solution in a 100 mL Erlenmeyer flask. The initial pH was adjusted to 6, and the suspension was agitated at 220 rpm and 298 K for 20 min. A parallel solution without added salt served as the control. After contact, a 2.0 mL aliquot was filtered through a 0.22 μm PES membrane, and the residual MB concentration was measured at 595 nm. Adsorption capacity and removal efficiency were calculated using Equations (1) and (2).

2.7 Regeneration and reuse experiments

Regeneration experiments began with adsorption using 0.020 g of CTAB@PG in 50 mL of 200 $mg \cdot L^{-1}$ MB solution at an initial pH of 6, 298 K, and 220 rpm for 20 min. The MB-loaded adsorbent was recovered and treated with 50 mL of 0.1 $mol \cdot L^{-1}$ NaOH at 298 K and 220 rpm for 60 min. The regenerated material was washed with DI water until neutral and dried at 60 °C. It was then contacted with a fresh 50 mL portion of 200 $mg \cdot L^{-1}$ MB solution at an initial pH of 6, 298 K, and 220 rpm for 20 min for the next adsorption step. Six consecutive adsorption–desorption cycles were performed. After each adsorption step, the residual MB concentration was determined by filtration and UV-Vis measurement as described in Section 2.4, and adsorption capacity and removal efficiency were calculated to evaluate performance retention.

3. Results and discussion

3.1 Characterization of adsorbent

FT-IR spectra were first examined to identify the organic groups introduced by CTAB treatment (Fig. 1(a)). The bands at 989 and 655 cm^{-1} are assigned to sulfate stretching and

bending vibrations, respectively, while the band near 1629 cm^{-1} is associated with the H–O–H bending vibration of water in the hydrated mineral constituents (Gong et al. 2020). The band at 879 cm^{-1} is assigned to carbonate absorption, in agreement with the $CaCO_3$ phase identified by XRD (So et al. 2020). The C–H stretching bands at 2825 and 2954 cm^{-1} arise from the alkyl groups of CTAB and support the introduction of organic components onto PG (Mostafa et al. 2023; Toledo-Jaldin et al. 2018).

Following identification of the organic groups, SEM was used to examine how treatment changed the exposed mineral surfaces. PG exhibited predominantly rhombohedral crystals with inclined columnar arrangements and relatively smooth surfaces (Fig. 1(b)) (Altaş et al. 2017). CTAB@PG showed a rougher, more irregular surface with particulate aggregates and less clearly defined crystal faces (Fig. 1(c)). This change indicates reorganization of the exposed surface morphology during CTAB-assisted treatment, producing a more irregular solid–water contact interface.

To determine whether the surface changes were accompanied by a change in mineral phases, XRD patterns were compared (Fig. 1(d)). Both samples exhibit the diffraction features of $CaSO_4 \cdot 2H_2O$ and $CaCO_3$ (Gong et al. 2020). The calcite reflections marked by triangles and the gypsum reflections marked by asterisks remain evident after treatment, with the principal peak positions retained. The preservation of these mineral reflections indicates that the main crystalline constituents persist after surface modification (Fig. 1(d)). Similar retention of mineral crystal structures after surfactant modification has been reported for zeolite (Hamoud et al. 2023) and palygorskite (Zhuang et al. 2017). The modest changes in relative peak intensities may reflect local dissolution–recrystallization during hydrothermal treatment (Wang et al. 2024).

With the principal crystalline phases retained, N_2 adsorption–desorption measurements were used to quantify changes in surface area and pore structure. BET surface areas and BJH

pore-size distributions are presented in Fig. 1(e), Fig. S1, and Table S1. Both materials exhibit type IV isotherms according to the IUPAC classification, indicating mesoporous characteristics (Sampieri et al. 2018; Thommes et al. 2015). The BET surface area decreases from 20.92 $m^2 \cdot g^{-1}$ for PG to 9.27 $m^2 \cdot g^{-1}$ for CTAB@PG, while pore volume decreases from 0.0989 to 0.0539 $cm^3 \cdot g^{-1}$. Thus, the rougher morphology observed by SEM is accompanied by a reduction in N_2-accessible surface area and pore volume. Surface-associated organic constituents can occupy pore space or restrict pore access during CTAB-assisted modification (Lu et al. 2023), offering an explanation for the reduced textural parameters.

Despite the lower BET surface area, CTAB@PG achieves substantially higher MB uptake than PG. The adsorption enhancement therefore results from more favorable dye–interface interactions rather than an increase in N_2-accessible surface area (Chamorro et al. 2024), demonstrating the effectiveness of interfacial functionalization in improving PG-based dye adsorption.

TGA was subsequently used to examine the thermal response of the organic and mineral constituents (Fig. 1(f)). Both samples exhibit minor mass losses beginning at approximately 100 °C, associated with retained moisture release and dehydration of hydrated constituents (Zhao et al. 2020). At 300 °C, the recorded mass losses are 2.9% for PG and 4.2% for CTAB@PG. The additional lower-temperature loss of CTAB@PG can partly arise from organic components introduced during modification (Luo et al. 2016; Mostafa et al. 2023). The pronounced loss at approximately 650–760 °C is compatible with decomposition of carbonate-containing constituents (Fernández-Penas et al. 2023), whose presence is also indicated by the carbonate FT-IR band and $CaCO_3$ diffraction features. Overall, CTAB@PG retains a broad thermal profile similar to PG, with an additional lower-temperature mass loss following organic modification.

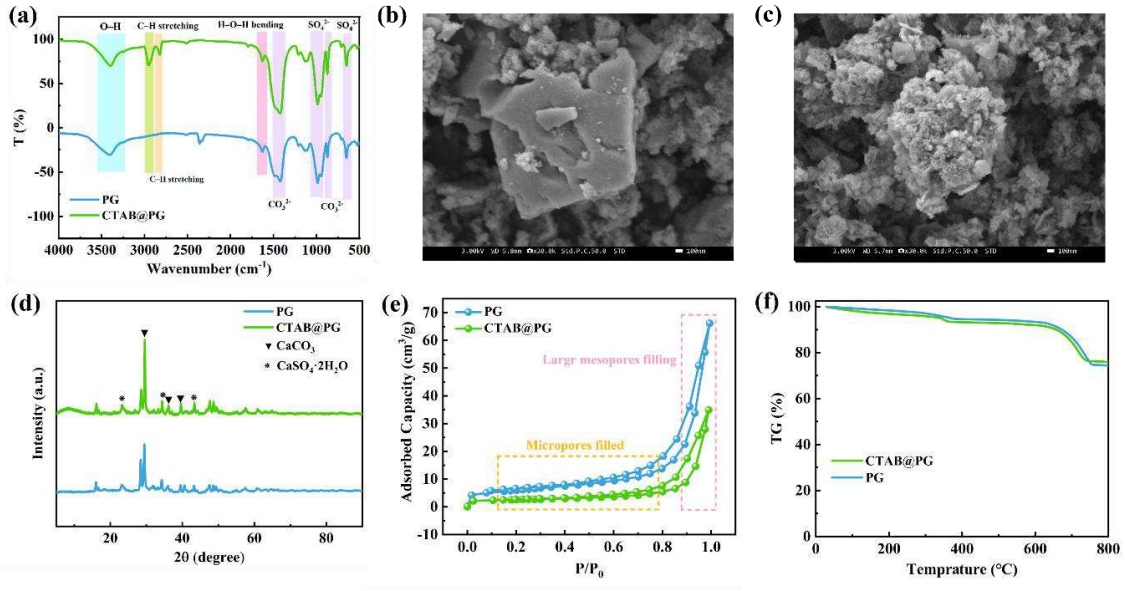


Fig. 1 (a) FT-IR spectra of PG and CTAB@PG; (b) SEM image of PG; (c) SEM image of CTAB@PG; (d) XRD patterns of PG and CTAB@PG; (e) N_2 adsorption-desorption (BET) isotherms of PG and CTAB@PG; (f) TG curves of PG and CTAB@PG

3.2 Batch adsorption experiments

3.2.1 Adsorption performance and effects of concentration and dosage

CTAB@PG achieved an MB uptake of 482.8 $mg \cdot g^{-1}$, compared with 215 $mg \cdot g^{-1}$ for PG under identical conditions (Fig. 2(a)). This corresponds to a 124.6% increase in uptake, or approximately 2.25 times the PG value, despite a 55.7% decrease in BET surface area from 20.92 to 9.27 $m^2 \cdot g^{-1}$ (Table S1). This substantial improvement demonstrates the effectiveness of CTAB modification in enhancing MB affinity at the solid–water interface. CTAB-derived cationic groups and organic regions promote the capture of anionic MB (Lu et al. 2023), enabling high uptake even with a reduced BET surface area. Reported capacities of selected MB adsorbents are summarized in Table S5 for comparison with the measured CTAB@PG uptake.

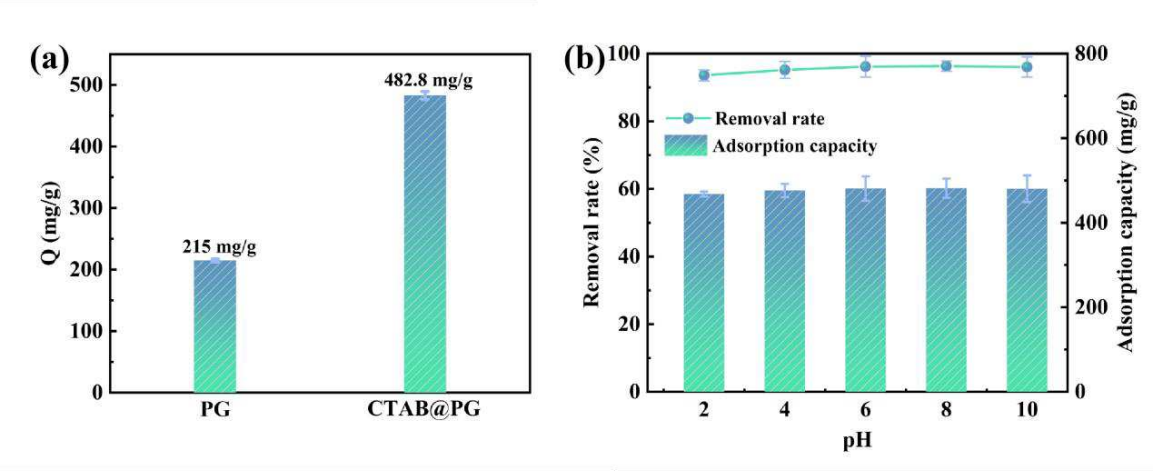


Fig. 2 (a) Comparison of the MB adsorption capacities of PG and CTAB@PG under identical conditions; (b) effect of initial pH on MB adsorption by CTAB@PG. Experimental conditions: adsorbent dosage, 0.02 g; solution volume, 50 mL; initial MB concentration, 200 mg·L^{-1}; temperature, 298 K; contact time, 20 min; pH = 6 for panel (a)

Increasing the initial MB concentration from 20 to 300 mg·L^{-1} increased uptake per unit mass while decreasing removal efficiency (Fig. 3(a)). At the fixed solution volume of 50 mL, this concentration range increases the initial MB inventory from 1 to 15 mg. Higher concentrations supply more dye and a larger concentration gradient for transfer toward the adsorbent (Huo et al. 2024; Sultana et al. 2022). At lower concentrations, a high fraction of the available MB is removed while the amount supplied limits the loading; as concentration increases, the fixed adsorbent mass captures more MB but removes a smaller fraction of the total inventory (Aggour et al. 2025). At the selected concentration of 200 mg·L^{-1}, the solution contains 10 mg of MB; 0.02 g of CTAB@PG adsorbs approximately 9.66 mg at an uptake of 482.8 mg·g^{-1}, corresponding to 96.6% removal. This concentration therefore permits high adsorbent loading while maintaining efficient removal of the available MB.

The dosage response shows how this dye inventory is distributed over the adsorbent mass. Increasing CTAB@PG from 0.01 to 0.05 g produced a modest increase in removal efficiency followed by a plateau, whereas uptake per unit mass decreased (Fig. 3(b)). For the fixed 10 mg MB inventory, the available dye per unit adsorbent mass decreases from 1000 to 200 mg·g^{-1} across this range. Additional adsorbent increases the number of accessible sites and improves capture (Huo et al. 2024). Once removal is already high, however, further addition

changes the total amount captured only modestly while distributing it over a larger mass, lowering the average loading and leaving more sites unoccupied (Huo et al. 2024; Ulatowska et al. 2021). Concentration and dosage thus govern the balance between dye supply and site availability. The selected dosage of 0.02 g gave 96.6% removal and 482.8 $mg \cdot g^{-1}$ uptake, balancing effective removal with efficient use of the adsorbent.

3.2.2 Effects of pH and coexisting ions

CTAB@PG maintained high MB uptake throughout the initial pH range of 2–10 (Fig. 2(b)). Uptake increased from pH 2 to 6 and then varied little up to pH 10; pH 6 gave the highest observed performance, with 482.8 $mg \cdot g^{-1}$ uptake and 96.6% removal under the working conditions. CTAB-derived quaternary ammonium groups provide cationic regions for association with the sulfonate groups of MB (Du et al. 2022; Elsherbiny et al. 2017). Their permanent ionic character offers a basis for sustaining dye association across a broad pH range. The broad pH response allows efficient MB removal without a narrow pH operating window, and pH 6 offers the highest measured uptake under near-neutral conditions.

To further examine the effects of dissolved ions on MB binding and the tolerance of the modified interface to salts, coexisting-ion experiments were conducted at 0–900 $mg \cdot L^{-1}$ (Fig. 3(e)). K^+, Zn^{2+}, and Ca^{2+} caused little change in MB uptake, indicating limited competition with anionic MB for the relevant binding regions (Patra et al. 2020). Added anions reduced uptake, with an inhibition order of $Cl^- \approx NO_3^- < SO_4^{2-}$ (Fig. 3(e)). The stronger sulfate inhibition is compatible with competition for CTAB-derived cationic regions (Shirzad-Siboni et al. 2015; Zheng et al. 2026). The contrasting cation and anion responses support an important role for electrostatic attraction in MB binding. Meanwhile, the retained high uptake across the tested salt concentrations demonstrates useful tolerance to the investigated ionic backgrounds.

3.2.3 Contact time and temperature responses

MB uptake was already high at the first sampling time of 1 min and then increased gradually toward a plateau (Fig. 3(c)). This response comprises rapid initial capture, a smaller increment during continued contact, and an approach to equilibrium. Readily accessible sites at the CTAB-modified interface favor the initial uptake (Wang et al. 2017). As MB is depleted from solution and these regions become occupied, the additional amount captured per unit time decreases. At 20 min, CTAB@PG achieved 482.8 $mg \cdot g^{-1}$ uptake and 96.6% removal; extending contact to 40 min produced only a small further increase. The high removal attained within 20 min and the limited gain thereafter demonstrate efficient MB capture over a short treatment period, supporting the selection of 20 min as the working contact time.

Raising the temperature over 298–353 K produced a modest increase in adsorption performance, followed by a plateau in the upper part of the range (Fig. 3(d)). With 200 $mg \cdot L^{-1}$ MB in 50 mL and 0.02 g of adsorbent, complete removal corresponds to 500 $mg \cdot g^{-1}$. The measured uptake of 482.8 $mg \cdot g^{-1}$ at 298 K is already close to this dye-supply limit, leaving little scope for an additional uptake increase under the same batch conditions. CTAB@PG therefore achieves near-complete MB removal at room temperature, while further heating gives only a limited performance gain. Operation at 298 K consequently combines high removal efficiency with a reduced need for external heating.

3.2.4 Regeneration and reuse performance

CTAB@PG retained high removal over six adsorption–desorption cycles using 0.1 $mol \cdot L^{-1}$ NaOH (Fig. 3(f)). Removal efficiency decreased overall from 96.6% initially to approximately 90% after the sixth cycle, with small fluctuations between cycles. Residual MB occupying adsorption sites after regeneration offers an explanation for the overall decline (Lu et al. 2023). Alkaline treatment facilitates anionic-dye release (Kitemangu et al. 2023), enabling reuse after washing and drying. Retention of approximately 93% of the initial

removal performance demonstrates that CTAB@PG tolerates repeated alkaline regeneration while preserving most of its MB adsorption functionality.

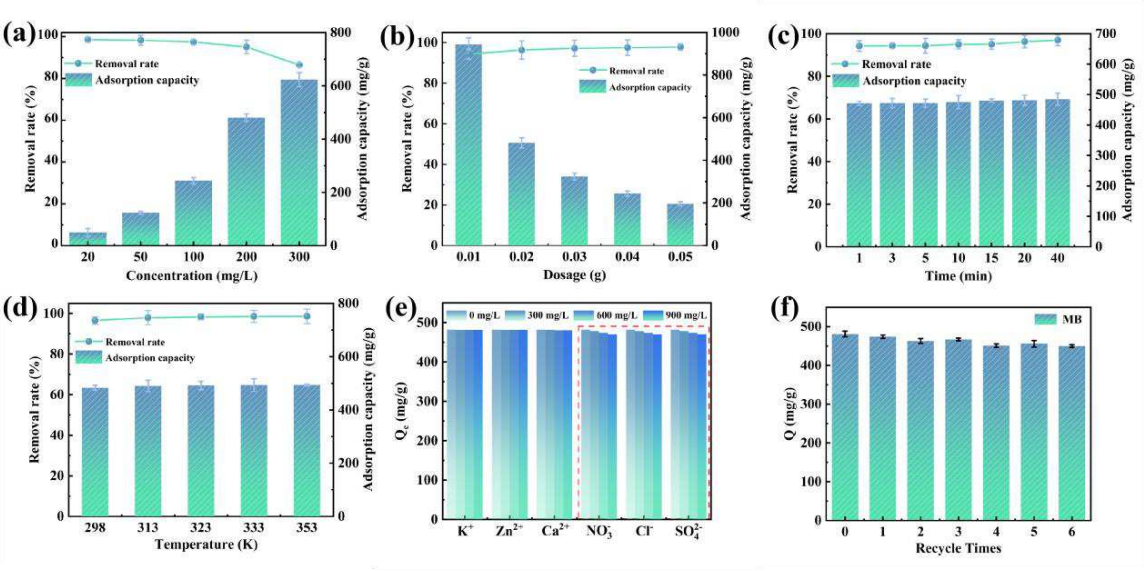


Fig. 3 Effects of key operational parameters on the batch adsorption performance of MB by CTAB@PG: (a) initial MB concentration; (b) CTAB@PG dosage; (c) contact time; (d) temperature; (e) influence of coexisting/competing ions; (f) reusability of CTAB@PG over six adsorption–desorption cycles. In panel (f), cycle 0 denotes the initial adsorption with fresh CTAB@PG, and cycles 1–6 denote adsorption after each regeneration. Error bars represent the standard deviation of triplicate measurements (n = 3)

3.3 Adsorption kinetics

To resolve the rapid MB uptake and subsequent transport behavior, the kinetic data at an initial concentration of 200 mg·L^{-1} and temperatures of 298, 313, and 333 K were analyzed using the PFO, PSO, and intraparticle diffusion models.

The PFO model (Equation (3)), PSO model (Equation (4)), and Weber–Morris intraparticle diffusion model (Equation (5)) were applied as follows (Huo et al. 2024; Hwang et al. 2015).

$$\ln(q_e - q_t) = \ln q_e - k_1 t \quad (3)$$

$$\frac{t}{q_t} = \frac{1}{q_e^2 k_2} + \frac{t}{q_e} \quad (4)$$

$$q_t = k_d t^{0.5} + C \quad (5)$$

In the expressions, k_1 and k_2 correspond to the rate constants of the PFO and PSO models, respectively, while q_e and q_t represent the adsorbed quantities at equilibrium and at time t, respectively. In the Weber-Morris model, k_d is the intraparticle diffusion rate constant, and C is the intercept related to the boundary-layer effect (Huo et al. 2024; Hwang et al. 2015).

Fig. 4(a,b) and Table 1 show that PSO gave higher R^2 values and equilibrium-capacity estimates closer to the experimental plateaus than PFO. Across the three temperatures, PSO predicted 485.44–495.05 $mg \cdot g^{-1}$ with R^2 values of 0.99997–0.99999, whereas PFO predicted 15.58–26.56 $mg \cdot g^{-1}$. At 298 K, the PSO estimate of 485.44 $mg \cdot g^{-1}$ differs from the measured uptake of 482.8 $mg \cdot g^{-1}$ by only 0.55%. The combination of close capacity agreement and high fitting coefficients supports PSO as the preferred description of the kinetic data.

The Weber–Morris plot at 333 K contains three fitted regions with non-zero intercepts (Fig. S2 and Table S2). The second region has the largest slope, 11.0647 $mg \cdot g^{-1} \cdot min^{-1/2}$, followed by a lower third-region slope of 0.9140 $mg \cdot g^{-1} \cdot min^{-1/2}$. The large intercepts of 456.81–487.76 $mg \cdot g^{-1}$ reflect the substantial uptake already attained at the earliest sampling times. Subsequent transport contributes a smaller additional uptake as the interface becomes occupied and the dissolved MB concentration decreases. Thus, most MB uptake is achieved during the initial rapid capture period, whereas later transport supplies a limited increment before equilibrium. This behavior demonstrates the ability of the modified interface to enrich MB rapidly and reach high removal within a short contact time.

Table 1 Kinetic parameters obtained from the PFO and PSO models for MB adsorption on CTAB@PG

Kinetic parameter	Temperature (K)		
	298	**313**	**333**
	Pseudo-first-order		
k_1 (min^{-1})	0.1473	0.2934	0.2307
$q_{e,cal}$ ($mg \cdot g^{-1}$)	15.58	25.13	26.56
R^2	0.8104	0.9896	0.9829
	Pseudo-second-order		
k_2 ($g \cdot mg^{-1} \cdot min^{-1}$)	0.0182	0.0227	0.0213
$q_{e,cal}$ ($mg \cdot g^{-1}$)	485.44	490.20	495.05
R^2	0.99997	0.99999	0.99999

3.4 Adsorption isotherms

Equilibrium isotherms describe MB partitioning between solution and CTAB@PG and its dependence on concentration and temperature (Agaguena et al. 2023; Aggour et al. 2025; Obayomi et al. 2022; Yang et al. 2022). The Langmuir model assumes monolayer adsorption on uniform sites (Equation (6)), while the Freundlich model represents a nonlinear uptake relationship associated with heterogeneous adsorption (Equation (7)). The Temkin model describes a coverage-dependent adsorption response (Equation (8)), and the D–R model provides a further representation of the equilibrium data (Equation (9)) (Aggour et al. 2025).

$$\frac{C_e}{q_e} = \frac{1}{q_{max} K_L} + \frac{C_e}{q_{max}} \quad (6)$$

$$\ln q_e = \ln K_F + \frac{1}{n} \ln C_e \quad (7)$$

$$q_e = B_T \ln A_T + B_T \ln C_e \quad (8)$$

$$\ln\left(\frac{q_e}{q_{ref}}\right) = \ln\left(\frac{q_s}{q_{ref}}\right) - K_{ad}\varepsilon^2 \quad (9)$$

In this context, q_e ($mg \cdot g^{-1}$) refers to the adsorption capacity at equilibrium, while C_e ($mg \cdot L^{-1}$) denotes the equilibrium concentration of the solute in solution. The Langmuir isotherm parameters include K_L ($L \cdot mg^{-1}$), which is the Langmuir affinity constant, and q_{max} ($mg \cdot g^{-1}$), representing the theoretical maximum adsorption capacity corresponding to

monolayer coverage. For the Freundlich model, K_F is the adsorption capacity coefficient, 1/n reflects the adsorption intensity, and n indicates the favorability and heterogeneity of the adsorption process. B_T (mg·g^{-1}) is the Temkin fitted slope in Equation (8), and A_T (L·mg^{-1}) is its binding parameter. K_{ad} (mol^2·J^{-2}) is the D–R fitted coefficient, and qs (mg·g^{-1}) is its fitted saturation-capacity parameter.

For reporting the D–R fit, the concentration-dependent potential is written with an explicit dimensionless concentration ratio:

$$\varepsilon = RT \ln\left(1 + \frac{C_{\mathrm{ref}}}{C_{\mathrm{e}}}\right) \tag{10}$$

Here, C_{ref} = 1 mg·L^{-1} is the fixed concentration normalization used in the D–R representation, and C_e is expressed in the same units. R = 8.314 J·mol^{-1}·K^{-1} and T is in K, giving ε in J·mol^{-1} and ε^2 in J^2·mol^{-2}. In Equation (9), q_{ref} = 1 mg·g^{-1} makes the loading ratios dimensionless. The solution standard state for the transfer thermodynamic calculations is defined in Section 3.5.

The isotherm fits at 298, 313, and 333 K are shown in Fig. 4(c–f), and the parameters are summarized in Table 2. Freundlich gave the highest R^2 values at all three temperatures (0.9926–0.9961), describing the nonlinear increase in uptake over the investigated concentration range. The fitted n values of 1.37–1.47 are consistent with favorable adsorption on a heterogeneous interface (Agaguena et al. 2023).

The equilibrium curves show higher MB uptake at elevated temperatures. In the Freundlich fits, K_F increased from 122.59 at 298 K to 210.40 at 333 K, while n varied between 1.37 and 1.47. These combined parameter changes describe the enhanced uptake over the investigated concentration range. Langmuir-fitted q_{max} values were 1035.44–1144.71 mg·g^{-1}, while the Temkin and D–R parameters provide additional comparisons of the equilibrium curves (Table 2). At a common equilibrium concentration, higher temperature

therefore favors MB uptake. These equilibrium relationships provide the data basis for subsequent thermodynamic analysis at fixed adsorption loadings.

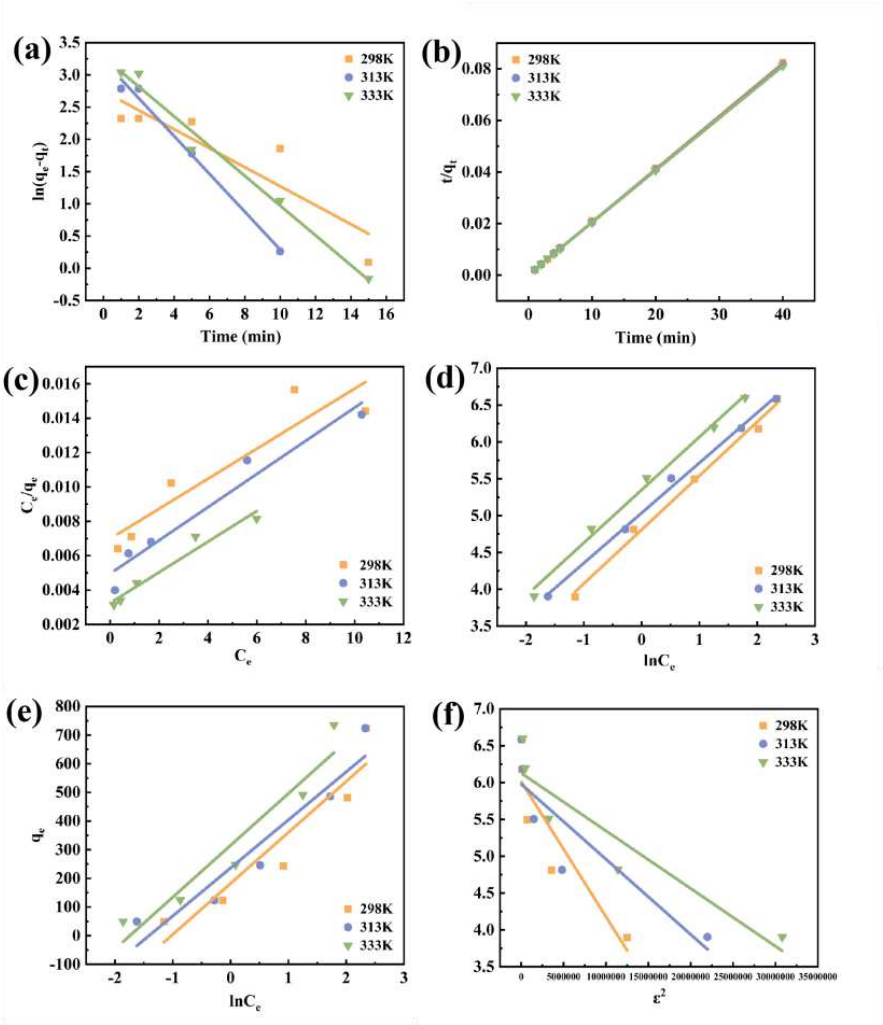


Fig. 4 Fitting curves of adsorption kinetics and isotherms for MB adsorption on CTAB@PG: (a) PFO model; (b) PSO model; (c) Langmuir model; (d) Freundlich model; (e) Temkin model; (f) D–R model. Experimental conditions: adsorbent dosage, 0.02 g; solution volume, 50 mL; pH = 6. For kinetic fitting, the initial MB concentration was 200 mg·L^{-1}. For isotherm fitting, experiments were conducted at different temperatures with a contact time of 20 min. In panel (f), ε^2 is expressed in J^2·mol^{-2}, and the ordinate labelled ln q_e denotes ln(q_e/q_{ref}), with q_{ref} = 1 mg·g^{-1}

Table 2 Key parameters of the adsorption isotherm model for MB adsorption on CTAB@PG

isotherm	parameters	Temperature (K)		
		298 K	**313 K**	**333 K**
Langmuir	q_{max} (mg·g^{-1})	1144.71	1035.44	1120.78
	K_L (L·mg^{-1})	0.1252	0.1947	0.2745
	R^2	0.8648	0.9516	0.9558
Freundlich	K_F	122.59	153.81	210.40
	n	1.37	1.47	1.39
	R^2	0.9933	0.9961	0.9926
Temkin	A_T (L·mg^{-1})	2.7846	4.0956	5.7067
	B_T (mg·g^{-1})	177.94	167.60	180.92
	R^2	0.8837	0.9078	0.9217
Dubinin-Radushkevich	q_s (mg·g^{-1})	408.86	395.83	459.00
	K_{ad} (mol^2·J^{-2})	1.834×10^{-7}	1.021×10^{-7}	7.835×10^{-8}
	R^2	0.8160	0.7810	0.8740

For Equation (7), q_e is expressed in mg·g^{-1} and the concentration in mg·L^{-1}. The units of K_F are (mg·g^{-1})(L·mg^{-1})$^{1/n}$.

3.5 Adsorption thermodynamics

To quantify the temperature dependence of adsorption equilibrium, thermodynamic parameters were evaluated at fixed MB loadings. Freundlich gave the highest fitting coefficients at all three temperatures (R^2 = 0.9926–0.9961) and was used for the primary analysis. Equation (7) was inverted to obtain C_e at specified q_e values at 298, 313, and 333 K. Langmuir calculations at the same loadings were used to test the consistency of the temperature response across the two isotherm representations. Concentrations were converted to mol·L^{-1} using M_w = 799.81 g·mol^{-1}, and R = 8.314 J·mol^{-1}·K^{-1} was used in the calculations.

Here, Δg_{ref} denotes the apparent differential molar Gibbs energy of transfer from the ideal solution standard state (C° = 1 mol·L^{-1}) to the adsorbed state at a specified q_e. This fixed-loading convention follows the structure of half-standard adsorption quantities (Everett 1972) and the equilibrium chemical-potential relation (Na 2020). A dilute-solution activity approximation and comparable background conditions between temperatures are assumed.

The derivation is provided in Online Resource 1, which also contains supplementary characterization, intraparticle diffusion analysis, thermodynamic calculations, and a literature comparison of MB adsorption capacities.

The regression and corresponding transfer parameters were calculated as follows:

$$\ln(\frac{C_e}{C^\circ}) = \frac{A}{T} + B \quad (11)$$

$$\Delta h_{ref} = RA \quad (12)$$

$$\Delta g_{ref} \equiv \mu_{ads} - \mu_{sol}^\circ \approx RT \ln(\frac{C_e}{C^\circ}) \quad (13)$$

$$\Delta s_{ref} = \frac{\Delta h_{ref} - \Delta g_{ref,fit}}{T} = -RB \quad (14)$$

A and B are the slope and intercept of $\ln(C_e/C^\circ)$ versus $1/T$ at fixed q_e. Enthalpy, entropy, and fitted Gibbs energy ($\Delta g_{ref,fit} = RA + RBT$) were obtained from the same regression. The plotting convention for Fig. S3 is detailed in the Supporting Information.

The Freundlich-derived isosteric transfer enthalpies were +17.16 to +17.64 kJ·mol^{-1} over 150–600 mg·g^{-1} (Fig. S3 and Table S3), demonstrating endothermic transfer throughout the common loading range of the three temperatures. At a given loading, the equilibrium concentration decreases as temperature rises, so the same uptake can be maintained at a lower dissolved MB concentration. Heating therefore favors MB partitioning to the adsorbed state even where the fixed-inventory batch experiment permits only a small additional uptake. At q_e = 300 mg·g^{-1}, Δh_{ref} was +17.40 kJ·mol^{-1} and Δs_{ref} was +160.93 J·mol^{-1}·K^{-1}; $\Delta g_{ref,fit}$ was −30.56, −32.97, and −36.19 kJ·mol^{-1} at 298, 313, and 333 K, respectively.

At the specified loadings, the negative transfer Gibbs energies indicate a lower chemical potential of adsorbed MB relative to the defined solution standard state. The positive transfer entropies are reported using the same reference convention.

Langmuir-derived standard parameters were calculated under ideal-site and dilute-solution assumptions (Chen et al. 2021) (Table S4(a)). At the same loadings, Langmuir-derived

isosteric transfer enthalpies were +17.61 to +17.96 kJ·mol^{-1}, differing from the Freundlich values by approximately 3% or less (Table S4(b,c)). Both representations therefore yield positive enthalpies with close numerical agreement throughout 150–600 mg·g^{-1}. This comparison demonstrates that the endothermic transfer conclusion is robust to the choice between the two isotherm representations, strengthening the thermodynamic interpretation of MB adsorption on CTAB@PG.

3.6 Interfacial adsorption mechanisms

CTAB modification improves MB adsorption by creating cationic binding regions and organic domains at the mineral–water interface, as illustrated in Fig. 5. FT-IR identifies the introduced alkyl groups, while XRD shows retention of the main mineral phases. Under identical adsorption conditions, uptake increases from 215 to 482.8 mg·g^{-1} despite a BET surface-area decrease from 20.92 to 9.27 m^2·g^{-1}. This enhancement demonstrates that improved dye affinity at the modified interface is the principal source of the performance gain. Surfactant functionalization supplies the quaternary ammonium groups and alkyl regions responsible for this altered interfacial environment (Dong et al. 2010; Lu et al. 2023; Mostafa et al. 2023).

Electrostatic attraction promotes MB binding through association of its sulfonate groups with CTAB-derived quaternary ammonium groups (Elsherbiny et al. 2017; Ettahiri et al. 2025; Wang et al. 2017). The adsorption experiments support this contribution: the tested cations have little effect, whereas added anions inhibit uptake, with SO_4^{2-} producing the strongest inhibition. Such competition is expected for anionic species binding to cationic regions. The permanent positive charge of quaternary ammonium groups also favors MB capture across the investigated pH range of 2–10. Alkaline elution releases adsorbed dye, and approximately 90% removal remains after six cycles, demonstrating that much of the MB-binding function can be restored through regeneration. Electrostatic binding at CTAB-derived

493 cationic regions therefore makes an important contribution to efficient and reusable MB
494 capture.

495 The C_{16} alkyl regions of CTAB provide an additional environment for hydrophobic
496 association with the aromatic portions of MB (Chamorro et al. 2024; Lu et al. 2023; Zheng et
497 al. 2026). The affinity of anionic dyes for CTAB-derived organic environments has also been
498 established in surfactant systems (Roik et al. 2021). In CTAB@PG, these alkyl regions
499 promote dye enrichment near the mineral surface and complement electrostatic binding at
500 quaternary ammonium groups. The chemically diverse mineral and surfactant regions provide
501 heterogeneous adsorption environments, as represented by the Freundlich equilibrium
502 response. The positive fixed-loading transfer enthalpies show that higher temperature favors
503 transfer to the adsorbed state; nevertheless, room-temperature operation already removes
504 most of the MB supplied under the working conditions. Overall, CTAB functionalization
505 produces an interface that combines strong MB affinity, rapid capture, a broad pH operating
506 range, and effective regeneration.

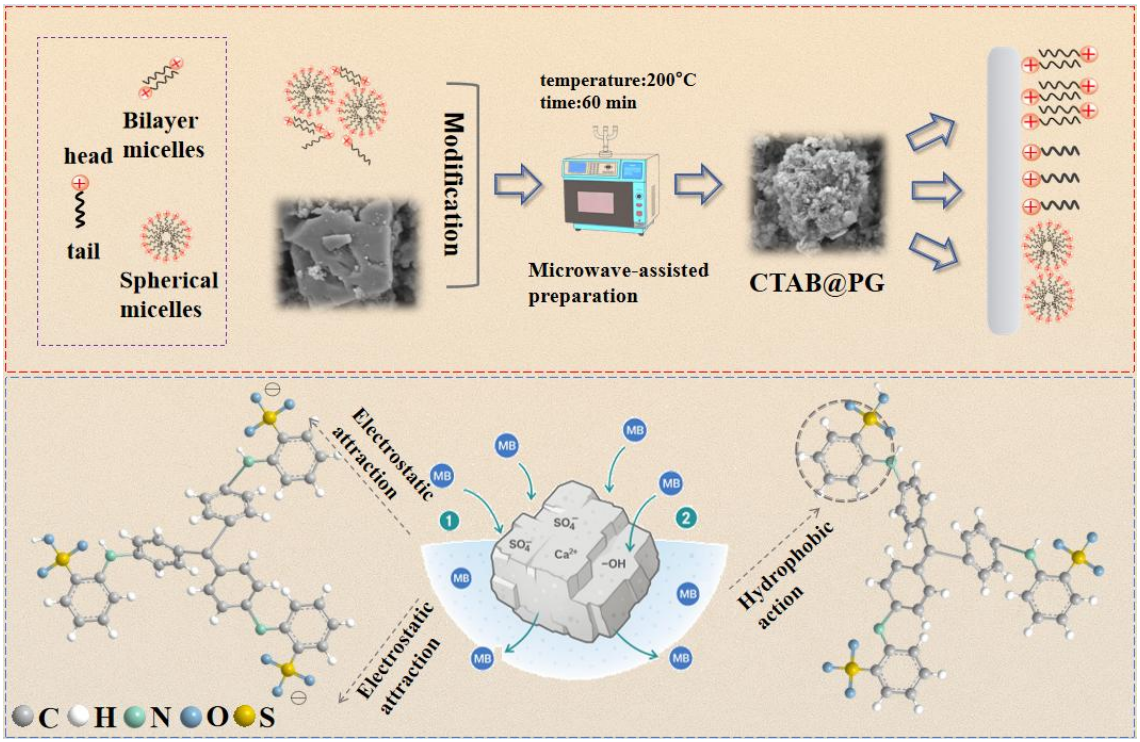


Fig. 5 Interfacial adsorption model for MB uptake by CTAB@PG. Labels 1 and 2 denote electrostatic attraction and hydrophobic association, respectively. CTAB arrangements in the upper panel schematically illustrate possible interfacial organization

4. Conclusions

Microwave-assisted CTAB treatment produced CTAB@PG with higher MB uptake than PG under identical adsorption conditions: 482.8 versus 215 $mg \cdot g^{-1}$, despite a BET surface-area decrease from 20.92 to 9.27 $m^2 \cdot g^{-1}$. At an initial MB concentration of 200 $mg \cdot L^{-1}$, a solution volume of 50 mL, a CTAB@PG dosage of 0.02 g, pH 6, 298 K, and 20 min, the measured removal efficiency was 96.6%. PSO better described the kinetic data, and Freundlich provided the preferred empirical representation of the equilibrium data. Freundlich- and Langmuir-based fixed-loading analyses yielded positive transfer enthalpies with relative differences of approximately 3% or less, demonstrating a consistent endothermic conclusion across the two representations. The pH, ion-interference, and regeneration results support electrostatic interactions at CTAB-derived cationic regions. Hydrophobic association with the alkyl components complements these interactions in the interfacial adsorption model.

Removal efficiency remained approximately 90% after six adsorption–desorption cycles. The combination of increased uptake, a broad initial-pH response, and retained performance after regeneration supports CTAB@PG as a reusable MB adsorbent under the tested aqueous conditions. These results illustrate a route for using PG as a substrate for dye-removal materials.

Statements and Declarations

Data availability

The data supporting the findings of this study are available from the corresponding authors upon reasonable request.

Competing interests

The authors have no relevant financial or non-financial interests to disclose.

Funding

This work was supported by the Project for Enhancing the Innovation Capacity of Shandong's Small and Medium-sized Technology-based Enterprises (Grant No. 2025TSGCCZZB0623).

List of Symbols

Symbol	Definition	Unit
C_0	Initial MB concentration	mg L^{-1}
C_e	Equilibrium MB concentration	mg L^{-1}
C_{ref}	Reference concentration used in the D–R representation	mg L^{-1}
C°	Solution standard concentration	mol L^{-1}
M_w	Molar mass of MB	g mol^{-1}
q_t	Adsorption capacity at time t	mg g^{-1}
q_e	Equilibrium adsorption capacity	mg g^{-1}
q_{max}	Langmuir theoretical maximum adsorption capacity	mg g^{-1}
q_s	D–R fitted saturation-capacity parameter	mg g^{-1}
q_{ref}	Reference adsorption capacity	mg g^{-1}
V	Solution volume	L
M	Adsorbent mass	g
T	Contact time	min
k_1	Pseudo-first-order rate constant	min^{-1}
k_2	Pseudo-second-order rate constant	g mg^{-1} min^{-1}
k_d	Intraparticle diffusion rate constant	mg g^{-1} $min^{-1/2}$
C	Weber–Morris intercept associated with the boundary-layer effect	mg g^{-1}
K_L	Langmuir affinity constant	L mg^{-1}
K_F	Freundlich adsorption-capacity coefficient	Model-dependent
N	Freundlich adsorption-intensity/heterogeneity parameter	Dimensionless
A_T	Temkin binding parameter	L mg^{-1}
B_T	Temkin fitted slope	mg g^{-1}
K_{ad}	Dubinin–Radushkevich fitted coefficient	mol^2 J^{-2}
ε	Polanyi adsorption potential	J mol^{-1}
R	Gas constant	J mol^{-1} K^{-1}
T	Absolute temperature	K
A, B	Slope and intercept of $\ln(C_e/C^\circ)$ versus 1/T at fixed q_e	K; dimensionless
θ	Fractional surface coverage	Dimensionless
ΔG_{ref}	Apparent differential molar Gibbs energy of transfer	kJ mol^{-1}
ΔH_{ref}	Differential molar transfer enthalpy	kJ mol^{-1}
ΔS_{ref}	Differential molar transfer entropy	J mol^{-1} K^{-1}
K_L°	Dimensionless Langmuir affinity constant	Dimensionless

Symbol	Definition	Unit
ΔG_L°	Langmuir-model standard Gibbs energy	kJ mol^{-1}
ΔH_L°	Langmuir-model standard enthalpy	kJ mol^{-1}
ΔS_L°	Langmuir-model standard entropy	J mol^{-1} K^{-1}

References

Agaguena A, Benbellat N, Khaoua O, Bendaikha T (2023) Kinetic adsorption of methyl blue dye from aqueous solution by PVC/PVC-based copolymer containing quaternary amine. Anal. Sci. 39:1371–1383. https://doi.org/10.1007/s44211-023-00356-y

Aggour YA, Kenawy E, Magdy M, Elbayoumy E (2025) Multifunctional copolymers for brilliant green dye removal: adsorption kinetics, isotherm and process optimization. Environ. Sci.: Adv. 4:787–808. https://doi.org/10.1039/d4va00404c

Ahmed MJ, Hameed BH, Anastopoulos I, Khanday WA (2026) Recent advances in surfactant-functionalized materials as adsorbents for enhanced remediation of synthetic dyes: a review. J. Taiwan Inst. Chem. Eng. 178:106398. https://doi.org/10.1016/j.jtice.2025.106398

Alotaibi AM, Aljabbab AA, Alajmi MS, Qadrouh AN, Farahat M, Abdel Khalek MA, Baioumy H, Alzahrani RY, Mana TH, Almutairi RS (2025) Utilization of phosphogypsum as sustainable adsorbent for removal of crystal violet dye from wastewater: kinetics, thermodynamics, and applications in textile effluent treatment. Sustainability 17:3320. https://doi.org/10.3390/su17083320

Altaş L, Balkaya N, Cesur H (2017) Pb(II) removal from aqueous solution and industrial wastewater by raw and lime-conditioned phosphogypsum. Int. J. Environ. Res. 11:111–123. https://doi.org/10.1007/s41742-017-0012-8

Bouzaabia S, Touati R, Kesraoui A (2025) Comparative study of thermal reflux and microwave-assisted functionalization of Luffa cylindrica with CTAB for enhanced dynamic biosorption of anionic dyes. Environ. Sci. Pollut. Res. 32:25108–25134. https://doi.org/10.1007/s11356-025-37111-x

Bulin C, Xiong Q, Zheng R, Li C, Ma Y, Guo T (2024) High efficiency removal of methyl blue using phytic acid modified graphene oxide and adsorption mechanism. Spectrochim. Acta A Mol. Biomol. Spectrosc. 307:123645. https://doi.org/10.1016/j.saa.2023.123645

Chamorro AF, Lerma TA, Palencia M (2024) CTAB surfactant promotes rapid, efficient, and simultaneous removal of cationic and anionic dyes through adsorption on glycerol/citrate polyester. Water 16:1860. https://doi.org/10.3390/w16131860

565 Chen T, Da T, Ma Y (2021) Reasonable calculation of the thermodynamic parameters from adsorption equilibrium
566 constant. J. Mol. Liq. 322:114980. https://doi.org/10.1016/j.molliq.2020.114980
567 Dang VL, Kieu TT, Nguyen TTT, Truong TTT, Hoang DT, Vu TLC, Nguyen TMT, Le TS, Doan THY, Pham TD
568 (2024) Surface modification of zeolite by cationic surfactant and the application on adsorptive removal of azo dye
569 Ponceau 4R. J. Mol. Struct. 1304:137619. https://doi.org/10.1016/j.molstruc.2024.137619
570 Deshmukh SM, Dhokpande SR, Sankhe A, Khandekar A (2025) Effluent wastewater technologies for textile industry:
571 a review. Rev. Inorg. Chem. 45:21–40. https://doi.org/10.1515/revic-2024-0046
572 Dong Y, Wu D, Chen X, Lin Y (2010) Adsorption of bisphenol A from water by surfactant-modified zeolite. J.
573 Colloid Interface Sci. 348:585–590. https://doi.org/10.1016/j.jcis.2010.04.074
574 Du J, Fan D, Dong Z, Yang X, Zhao L (2022) Fabrication of quaternized sisal fiber by electron beam radiation and its
575 adsorption of indigo carmine from aqueous solution. Cellulose 29:5137–5149. https://doi.org/10.1007/s10570-
576 022-04568-9
577 Elsherbiny AS, El-Hefnawy ME, Gemeay AH (2017) Linker impact on the adsorption capacity of
578 polyaspartate/montmorillonite composites towards methyl blue removal. Chem. Eng. J. 315:142–151.
579 https://doi.org/10.1016/j.cej.2017.01.002
580 Ettahiri Y, Aziz A, Felaous K, Bouddouch A, Akhsassi B, Bouna L, Benlhachemi A, Pérez-Villarejo L (2025)
581 Enhanced adsorption of Orange G dye using activated diatomite: a novel functionalization approach. Mater. Adv.
582 6:5171–5183. https://doi.org/10.1039/D5MA00536A
583 Everett DH (1972) Manual of symbols and terminology for physicochemical quantities and units, Appendix II:
584 definitions, terminology and symbols in colloid and surface chemistry. Pure Appl. Chem. 31:577–638.
585 https://doi.org/10.1351/pac197231040577
586 Fernández-Penas R, Verdugo-Escamilla C, Triunfo C, Gärtner S, D'Urso A, Oltolina F, Follenzi A, Maoloni G,
587 Cölfen H, Falini G, Gómez-Morales J (2023) A sustainable one-pot method to transform seashell waste calcium
588 carbonate to osteoinductive hydroxyapatite micro-nanoparticles. J. Mater. Chem. B 11:7766–7777.
589 https://doi.org/10.1039/D3TB00856H
590 Gong S, Li X, Song F, Lu D, Chen Q (2020) Preparation and application in HDPE of nano-CaSO4 from
591 phosphogypsum. ACS Sustain. Chem. Eng. 8:4511–4520. https://doi.org/10.1021/acssuschemeng.9b07632
592 Hamoud MA, Abo-Zahra SF, Attia MA, Someda HH, Mahmoud MR (2023) Efficient adsorption of cesium cations
593 and chromate anions by one-step process using surfactant-modified zeolite. Environ. Sci. Pollut. Res. 30:53140–
594 53156. https://doi.org/10.1007/s11356-023-25644-y

595 Hidayat E, Sarbani NMM, Susanto HB, Situngkir YV, Chrisandi MW, Samitsu S, Mitoma Y, Yonemura S, Harada H
596 (2024) Performance of hydrogel beads composites derived from sodium alginate-cetyltrimethylammonium
597 bromide toward Congo red dye adsorption from aqueous solution. Desalin. Water Treat. 318:100313.
598 https://doi.org/10.1016/j.dwt.2024.100313

599 Hosny NM, Gomaa I, Elmahgary MG (2023) Adsorption of polluted dyes from water by transition metal oxides: a
600 review. Appl. Surf. Sci. Adv. 15:100395. https://doi.org/10.1016/j.apsadv.2023.100395

601 Hu W, Chen J, Zhang J (2025) PEI-grafted graphene oxide modified phosphogypsum for the adsorption and removal
602 of heavy metals and dyes in wastewater. Water Res. 286:124236. https://doi.org/10.1016/j.watres.2025.124236

603 Huo L-Z, Guo C-F, Gong Z-X, Xu H, Yang X-J, Wang Y-X, Luo X-P (2024) Preparation of aminated sodium
604 lignosulfonate and efficient adsorption of methyl blue dye. Materials 17:1046.
605 https://doi.org/10.3390/ma17051046

606 Hwang K-J, Shim W-G, Kim Y, Kim G, Choi C, Kang SO, Cho DW (2015) Dye adsorption mechanisms in TiO2
607 films, and their effects on the photodynamic and photovoltaic properties in dye-sensitized solar cells. Phys. Chem.
608 Chem. Phys. 17:21974–21981. https://doi.org/10.1039/C5CP03416G

609 Kitemangu A, Vegi MR, Malima NM (2023) Biosorption of Congo red dye from aqueous solution using adsorbent
610 prepared from Vangueria infausta fruit pericarp. Adsorpt. Sci. Technol. 2023:4319053.
611 https://doi.org/10.1155/2023/4319053

612 Lin X, Zhou Q, Xu H, Chen H, Xue G (2024) Advances from conventional to biochar enhanced biotreatment of
613 dyeing wastewater: a critical review. Sci. Total Environ. 907:167975.
614 https://doi.org/10.1016/j.scitotenv.2023.167975

615 Lu M, Wang Y, Yu J, Li D, Zhao Q, Chi R (2023) Treating waste with waste: adsorption of anionic dyes in
616 wastewater with surfactant-modified phosphogypsum. Environ. Res. 237:116963.
617 https://doi.org/10.1016/j.envres.2023.116963

618 Luo W, Inoue A, Hirajima T, Sasaki K (2016) Sequential modification of montmorillonite with dimethyl dioctadecyl
619 ammonium chloride and benzyl octadecyl dimethyl ammonium chloride for removal of perchlorate. Microporous
620 Mesoporous Mater. 233:117–124. https://doi.org/10.1016/j.micromeso.2015.12.030

621 Mostafa AG, Abd El-Hamid AI, Akl MA (2023) Surfactant-supported organoclay for removal of anionic food dyes in
622 batch and column modes: adsorption characteristics and mechanism study. Appl. Water Sci. 13:163.
623 https://doi.org/10.1007/s13201-023-01959-6

624 Na C (2020) Size-controlled capacity and isocapacity concentration in Freundlich adsorption. ACS Omega 5:13130–
625 13135. https://doi.org/10.1021/acsomega.0c01144

626 Obayomi KS, Lau SY, Akubuo-Casmir D, Yahya MD, Auta M, Bari ASMF, Oluwadiya AE, Obayomi OV, Rahman
627 MM (2022) Adsorption of endocrine disruptive Congo red onto biosynthesized silver nanoparticles loaded on
628 Hildegardia barteri activated carbon. J. Mol. Liq. 352:118735. https://doi.org/10.1016/j.molliq.2022.118735

629 Patra C, Gupta R, Bedadeep D, Narayanasamy S (2020) Surface-treated acid-activated carbon for adsorption of
630 anionic azo dyes from single and binary adsorptive systems: a detail insight. Environ. Pollut. 266:115102.
631 https://doi.org/10.1016/j.envpol.2020.115102

632 Roik NV, Belyakova LA, Dziazko MO (2021) Solubilization of azo dyes by cetyltrimethylammonium bromide
633 micelles as structure control factor at synthesis of ordered mesoporous silicas. J. Mol. Liq. 328:115451.
634 https://doi.org/10.1016/j.molliq.2021.115451

635 Sahu A, Poler JC (2024) Removal and degradation of dyes from textile industry wastewater: benchmarking recent
636 advancements, toxicity assessment and cost analysis of treatment processes. J. Environ. Chem. Eng. 12:113754.
637 https://doi.org/10.1016/j.jece.2024.113754

638 Sampieri A, Pérez-Osorio G, Hernández-Espinosa MÁ, Ruiz-López II, Ruiz-Reyes M, Arriola-Morales J, Narváez-
639 Fernández RI (2018) Sorption of BTEX on a nanoporous composite of SBA-15 and a calcined hydrotalcite. Nano
640 Converg. 5:21. https://doi.org/10.1186/s40580-018-0153-2

641 Shao C, Ma M, Zhu X, Xing B, Zhang C, Du D, Chi R (2026) Phosphogypsum as an industrial byproduct: a critical
642 review on environmental risks, remediation, and resource recovery-circular challenges. Process Saf. Environ.
643 Prot. 208:108456. https://doi.org/10.1016/j.psep.2026.108456

644 Shirzad-Siboni M, Khataee A, Hassani A, Karaca S (2015) Preparation, characterization and application of a CTAB-
645 modified nanoclay for the adsorption of an herbicide from aqueous solutions: kinetic and equilibrium studies. C.
646 R. Chim. 18:204–214. https://doi.org/10.1016/j.crci.2014.06.004

647 So RT, Blair NE, Masterson AL (2020) Carbonate mineral identification and quantification in sediment matrices
648 using diffuse reflectance infrared Fourier transform spectroscopy. Environ. Chem. Lett. 18:1725–1730.
649 https://doi.org/10.1007/s10311-020-01027-4

650 Sultana AI, Chambers C, Ahmed MMN, Pathirathna P, Reza T (2022) Multifunctional loblolly pine-derived
651 superactivated hydrochar: effect of hydrothermal carbonization on hydrogen and electron storage with carbon
652 dioxide and dye removal. Nanomaterials 12:3575. https://doi.org/10.3390/nano12203575

653 Thommes M, Kaneko K, Neimark AV, Olivier JP, Rodriguez-Reinoso F, Rouquerol J, Sing KSW (2015)
654 Physisorption of gases, with special reference to the evaluation of surface area and pore size distribution (IUPAC
655 Technical Report). Pure Appl. Chem. 87:1051–1069. https://doi.org/10.1515/pac-2014-1117

Toledo-Jaldin HP, Blanco-Flores A, Sánchez-Mendieta V, Martín-Hernández O (2018) Influence of the chain length of surfactant in the modification of zeolites and clays. Removal of atrazine from water solutions. Environ. Technol. 39:2679–2690. https://doi.org/10.1080/09593330.2017.1365097

Ulatowska J, Stala Ł, Polowczyk I (2021) Comparison of Cr(VI) adsorption using synthetic schwertmannite obtained by Fe3+ hydrolysis and Fe2+ oxidation: kinetics, isotherms and adsorption mechanism. Int. J. Mol. Sci. 22:8175. https://doi.org/10.3390/ijms22158175

Vaid S, Kaur V, Sharma S, Singh A, Vaid B, Arya RK, Verros GD (2024) Utilizing local waste: sustainable adsorption of Reactive Blue 235 on surfactant-modified bamboo fibers. J. Eng. 2024:8706884. https://doi.org/10.1155/2024/8706884

Wang H, Jia S, Wang H, Li B, Liu W, Li N, Qiao J, Li C-Z (2017) A novel-green adsorbent based on betaine-modified magnetic nanoparticles for removal of methyl blue. Sci. Bull. 62:319–325. https://doi.org/10.1016/j.scib.2017.01.038

Wang Y, Cao H, Wang X, Jiang J (2024) Experimental and theoretical investigation on the mechanism of cationic surfactants-assisted phosphogypsum crystal transformation. Surf. Interfaces 47:104211. https://doi.org/10.1016/j.surfin.2024.104211

Yang H, Li J, Hu S, Liu Y, Peng C, Deng C, Chen Q, Hu T, Shan S, Zhi Y, Su H, Jiang L (2022) Fe-doped zeolitic imidazolate framework-8 as superior adsorbent for enhanced ciprofloxacin removal from aqueous solution. Appl. Surf. Sci. 586:152687. https://doi.org/10.1016/j.apsusc.2022.152687

Zhao L, Zhang Q, Li X, Ye J, Chen J (2020) Adsorption of Cu(II) by phosphogypsum modified with sodium dodecyl benzene sulfonate. J. Hazard. Mater. 387:121808. https://doi.org/10.1016/j.jhazmat.2019.121808

Zheng S, Bai M, Li Y, He R, Wang W, Feng Y, Wang H, Liu F, Fang Z (2026) Enhanced adsorption of xylenol orange by CTAB-functionalized tomato-derived biochar: mechanisms and performance evaluation. Molecules 31:708. https://doi.org/10.3390/molecules31040708

Zhuang G, Wu H, Zhang H, Zhang Z, Zhang X, Liao L (2017) Rheological properties of organo-palygorskite in oil-based drilling fluids aged at different temperatures. Appl. Clay Sci. 137:50–58. https://doi.org/10.1016/j.clay.2016.12.015

Supplementary Files

This is a list of supplementary files associated with this preprint. Click to download.

- ChemicalPapersSupplementaryInformation.docx